NUMERICAL INVESTIGATION OF ROTOR DOWNWASH EFFECT ON FREE-FLIGHT ROCKETS LAUNCHED FROM A HELICOPTER

Bum Seok Lee[*], Mun Seung Jung[*], Oh Joon Kwon[**]

Korea Advanced Institute of Science and Technology (KAIST)
335 Gwahangno, Yuseong-gu, Daejeon 305-701, KOREA

Abstract

Numerical simulation of unsteady flows around helicopters was conducted to investigate the aerodynamic interference between main rotor and other components. The effect of rotor downwash on the behavior of air-launched free-flight rockets and their plume was also investigated. For this purpose, a three-dimensional inviscid flow solver has been developed based on unstructured meshes. An overset mesh technique was used to describe the relative motion between main rotor, tail rotor, fuselage, and launched rockets. The flow solver was also coupled with six degree-of-freedom equations of motion to predict the trajectory of free-flight rockets air-launched from a helicopter. For the validation of the flow solver, calculations were made for the rotor-fuselage aerodynamic interaction of the ROBIN (ROtor Body INteraction) configuration and for a complete UH-60 helicopter configuration consisted of main rotor, fuselage, and tail rotor. Comparison of the computational results was made with available experimental data. It was found that significant mutual interference exists between main rotor and other components as confirmed by the unsteady flow characteristics and the aerodynamic loads. Simulation of air-launched rockets from an UH-60 helicopter showed that rotor downwash has non-negligible effect on the trajectory of the rocket and its plume development, which may potentially affect the safety and the reliability of other equipments.

1. INTRODUNCTION

In modern battlefields, helicopters are frequently used as a platform of military weapon systems, such as free-flight rockets and guided missiles. These weapon systems, when air-launched from a helicopter, initially travel at relatively low speed, and thus at this initial stage the trajectory and the initial stability of the rocket may be significantly influenced by the induced downwash of the main rotor. In addition, the high-temperature plume flow from the nozzle exit of the launched rocket is also affected by the rotor wake, which may cause potential damage to external equipments and other rockets remaining inside the launcher tubes. Thus it is important to estimate the rotor downwash accurately and to investigate its mutual interference with other helicopter components, including tail rotor, fuselage, rocket launcher, and traveling rockets.

Numerical study about external projectiles and their plume effect was previously conducted for fixed-wing aircrafts. Shanks and Ahmad [1] used a 3-D dynamic structured overset mesh method to simulate the aerodynamics, missile dynamics, and plume of a finless missile separating from a wing in transonic flow. A powered missile separation case was considered to examine the influence of the missile and plume on the wing. Cavallo, Sinha and Feldman [2] performed numerical simulation of rocket stage separation and missiles launched from a fighter aircraft. In their studies, a three-dimensional unstructured mesh Navier-Stokes flow solver was used, coupled with a parallel moving mesh technique. The accuracy of the solution was enhanced by conducting solution-adaptive mesh refinement.

For helicopters, a study about the aerodynamic interference between the main rotor and a launched rocket was experimentally conducted by Taylor and Landgrebe [3] for a model AH-1G helicopter operating in low speed forward flight. In their study, the wake flow induced by the rotor was visualized, and its effect on the trajectory of the fired rocket was measured at various operating conditions.

Wei and Gestvang [4] performed numerical simulation of the trajectory of Penguin missiles launched from a SH-2G helicopter. For this purpose, a panel method was used to find fuselage airflow interference, and the rotor wake induced interference velocity was computed by a vortex wake module. The measured flow field data was converted to interference coefficients and incorporated into a six degree-of-freedom(DOF) trajectory simulation system. The trajectory simulation was made at various weather and operating conditions.

Even though, those previous studies provide some insight about the behavior of free-flight rockets released from the mother vehicle, a more detailed study based on modern CFD techniques is needed. This is particularly true for the free-flight rockets air-launched from a helicopter, because the flowfield around a helicopter is much more complicated than fixed-wing aircrafts due to the mutual interference of various components, and its effect on the trajectory of launched rockets and the plume development has not been fully understood so far.

In the present study, a numerical method has been developed for the simulation of unsteady flows around a complete helicopter configuration, including free-flight rockets, based on unstructured meshes. To describe the relative motion between main rotor, fuselage, tail rotor,

[*] Graduate Research Assistant, Department of Aerospace Engineering.
[**] Corresponding author, Professor, Department of Aerospace Engineering, email: ojkwon@kaist.ac.kr.

and moving rockets, an overset mesh technique was adopted. The flow solver has been coupled with six degree-of-freedom dynamic equations of motion to predict the trajectory of air-launched rockets. For the validation of the present flow solver, calculations were made for the rotor-fuselage interaction flow of the ROBIN configuration, and the results were compared with experimental data. Then the mutual interference between main rotor, fuselage, and tail rotor of a UH-60 helicopter configuration was investigated, and the flowfield and the airloads on the rotor were examined. Finally, simulation of the free-flight rockets air-launched from a UH-60 helicopter was made, and the behavior of the rockets with and without canard and fin installation was studied. The effect of rotor downwash on rocket plume development and other helicopter components were also assessed.

2. NUMERICAL METHOD

2.1 Spatial Discretization and Time Integration

The equations governing three-dimensional, inviscid, unsteady, compressible flows are the Euler equations, which can be recast in an integral form for a bounded domain V with boundary ∂V;

$$\frac{\partial}{\partial t}\iiint_V Q\,dV + \iint_{\partial V} F(Q)\cdot\vec{n}\,dS = 0 \tag{1}$$

where $Q=[\rho, \rho u, \rho v, \rho w, e_0]$ is the solution vector of the conservative variables for the mass, momentum and energy equations. The governing equations were discretized using a vertex-centered finite-volume method. The flow domain was divided into a finite number of control volumes surrounding each vertex, which are made of a non-overlapping median-dual cell whose boundary surfaces are defined by the cell centroid, face centroid, and mid-point of the edge. The inviscid flux term, $F(Q)$, was computed using Roe's flux-difference splitting scheme [5]. The flow variables at each dual face were computed by using a linear reconstruction technique to achieve second-order spatial accuracy. In this approach, the face value of the primitive variables was calculated from those at the dual face using the averaged solution gradient of each control volume obtained from a least-square procedure.

An implicit time integration algorithm based on a linearized second-order Euler backward differencing was used to advance the solution in time. The linear system of equations was solved at each time step using a point Gauss-Seidel method.

2.2 Boundary Condition

At the far-field boundary, the characteristic boundary condition was applied. On the solid surface of body, the flow tangency condition was imposed.

For the simulation of rocket plume, an incoming flow boundary was set at the rocket nozzle throat. The values of total pressure and total temperature were set the same as those inside the combustion chamber known from measurement. The flow velocity was set to local Mach number of one, and other flow quantities were evaluated based on the isentropic relation. For the simplicity of the calculation, the gas was assumed to be hot air, and chemical reaction was not allowed.

2.3 Unstructured Overset Mesh Technique

To handle multiple bodies in relative motion effectively, an overset mesh scheme was adopted [6]. For the overset mesh method, a search procedure is needed for the identification of donor cells that contain the verticies from the opposite overlapping mesh block. For unstructured meshes, the search should be performed for all nodes of all mesh blocks, because the nodes and the cells are randomly distributed. To overcome the large computational overhead involved in this search process, a fast and robust neighbor-to-neighbor search technique was implemented by utilizing the property of linear shape functions [7]. Under parallel computing environment, the search may develop across the subdomain block boundary, and the amount of data information assigned to each processor may change at each iteration. To handle this varying amount of calculation load efficiently, a new data structure for parallel distributed memory machine was implemented.

Once the search process is completed, the information is used for clarifying the node type and for determining the weighting factors necessary for interpolation. In the present overset mesh method, a distance-to-wall technique [8] was implemented for grouping active nodes and non-active nodes. Hole cutting for determining cell types as either active, interpolation, or non-active was made based on the number of active nodes assigned to each tetrahedral cell. Then interpolation and transfer of the flow variables were made between adjacent mesh blocks. In order to reduce the error involved in the interpolation, both the cell containing the interpolation receiver and also the neighboring cells enclosing that cell were considered.

2.4 Thrust Calculation

The thrust of the launched rocket by the plume development can be calculated by using the following thrust equation at the nozzle exit.

$$\begin{aligned} Thrust &= (P_e - P_\infty)A_e + \dot{m}U_e \\ &= \int (P_e - P_\infty)dA_e + \int \rho_e \cdot \overrightarrow{u_e}(\overrightarrow{u_e}\cdot\vec{n})dA_e \end{aligned} \tag{2}$$

2.5 Trajectory Simulation

To describe the trajectory of free-flight rockets, six degree-of-freedom dynamic equations of motion were couple with the flow solver. These ordinary differential equations were integrated in time by using the 4th order Runge-Kutta method. The effect of gravitational acceleration was also included in the trajectory calculation.

2.6 Parallel Computation

In order to reduce large computational time to handle large number of cells, a parallel algorithm based on a domain decomposition strategy was adopted. The load balancing between processors was achieved by partitioning the global computational domain into local subdomains using the MeTiS libraries. The Message Passing Interface was used to transfer the flow variables across the subdomain boundary. This load balancing was made for each sub-block mesh, and thus was not strictly

achieved for the global computational domain. All calculations were made on Linux-based PC clusters.

3. RESULTS AND DISCUSSION

Initially, calculation was made for the ROBIN rotor-fuselage configuration to validate the capability of the present flow solver for accurately predicting induced downwash by the main rotor and the rotor-fuselage aerodynamic interference phenomena. Next, a full configuration of UH-60 helicopter composed of main rotor, tail rotor, and fuselage was calculated to demonstrate the ability of the present method for simulating complete rotorcraft configurations. Finally, application was made to simulate the initial behavior and the trajectory of free-flight rockets launched from a full configuration UH-60 helicopter.

3.1 ROBIN Configuration

The ROBIN [9] is a generic rotor-fuselage configuration consisted of a super ellipse-shaped fuselage and four blades. The blade has a rectangular platform shape with an NACA 0012 airfoil section, and is linearly twisted by -8 degrees from blade root to tip. The aspect ratio of the blade is 12.98, and the root cut-out is 0.24R. The operating blade tip Mach number is 0.523. Among the various experimental conditions, the one at a very low advance ratio of 0.012 was chosen, because the rotor is in near hover. The measured time-averaged thrust coefficient of the rotor is 0.0063.

The computational overset mesh consisted of five mesh blocks. The main block covers the complete computational domain and the fuselage. The four sub-blocks cover each of the four rotor blades. The mesh was constructed with 604,153 vertices for the main block and 143,654 vertices for each sub-block. The total number of cells used was 6,498,680. In Fig. 1, the mesh distribution on the fuselage and blade surface and at the fuselage symmetric plane is presented. It is shown that small cells are distributed around the blades and the fuselage where the inference between the two components becomes most severe.

For the accurate simulation of rotor downwash flow, the blade collective pitch setting was adjusted until the calculated thrust matched to that of the experiment. The resultant blade collective pitch angle was 6.64 degrees, while the experimentally measured value was 8.8 degrees. Since the advance ratio is very small, rotor trim was conducted for the collective pitch angle only, and longitudinal and lateral cyclic pitch angles were used as provided from the experiment.

In Fig. 2, unsteady pressure variations along the top center line of the fuselage are compared with experiment at four selected surface points. The presented experimental pressure data were shifted in phase by 252 degrees from the original data [10]. Although there is small deviation in the phase from the experiment, the overall results are in good agreement with the experiment for both magnitude and phase.

In Fig. 3, unsteady pressure variations around the fuselage at the streamwise station x/l=0.9 are compared with the experiment at four selected points; two at the advancing side of the fuselage, D23 and D25, and the other two at the retreating side, D4 and D19. It is shown that the results compare reasonably well with the experiment, even though the phase difference still exists between the two results.

The time-averaged pressure distributions around the fuselage at two selected streamwise locations are compared with the experiment in Fig. 4. It is shown that good comparison is made at X/l=0.35 located ahead of the pylon. At the location downstream of the pylon, X/l=1.17, the overall agreement is fair, and some deviation is observed, particularly at negative z-locations. This is presumably due to the fact that these points are under the fuselage and are affected by the structure supporting the fuselage in the experiment, which is not modeled in the present simulation.

In Fig. 5, the instantaneous vorticity contours are presented at the fuselage symmetric plane. It is shown that the fuselage is completely submersed inside the rotor wake, and the tip vortex directly impinges to the fuselage, inducing strong rotor-fuselage interaction.

3.2 Complete UH-60 Configuration

As the second validation, the mutual interaction of main rotor, fuselage, and tail rotor was simulated for a complete UH-60 helicopter configuration. The main rotor is consisted of four blades that are made of SC-1095 and SC-1094 airfoil sections, and have an aspect ratio of 15.51 [11]. The blade of the tail rotor has an aspect ratio of 3.1, and the gear ratio of tail rotor to main rotor is 4.62 [12]. For the simplicity of the calculation, the engine casing and the landing gear were not modeled. The calculation was made for a hovering flight condition at a blade tip Mach number of 0.65 and a collective pitch angle of 9.2° with C_T/σ=0.085.

In this calculation, a simplified trim was made such that the torque produced by the main rotor is compensated by the tail rotor. For this purpose, the collective pitch angle of the tail rotor blade was adjusted until the main rotor torque C_q obtained experimentally [13], $6.7732X10^{-4}$, was cancelled by the thrust of the tail rotor multiplied by the moment arm from the axis of the main rotor to the tail rotor. The resultant collective pitch angle of the tail rotor blade was 18.8°, which provided an anti-torque C_q of $6.7372X10^{-4}$.

Figure 6 shows the mesh distribution on the surface of the UH–60 configuration and at the fuselage symmetric cutting plane. The computational overset mesh contained 504,488, 679,940, and 110,040 vertices in each mesh blocks for fuselage, main rotor, and tail rotor, respectively. It is shown that fine cells are distributed around the main rotor, tail rotor, and fuselage to capture the wake and the aerodynamic interaction phenomena more accurately. The total number of cells used was 6,902,466.

In Fig. 7, the downwash inflow contours at one chord length above the rotor disk plane is presented. It shows that the contours are slightly distorted near Ψ = 0 °, showing higher inflow in this region. This is because strong sidewise flow is pumped by the tail rotor, which sucks in substantial amount of downwash flow from the main rotor. As a result, the magnitude of downwash near the tail rotor along the rotor azimuth angle Ψ = 0 ° increased.

In Fig. 8, the downwash distribution along Ψ = 0 ° at one chord length above the rotor disk plane is presented. The result is also compared with that of the rotor-fuselage

configuration without tail rotor. The figure shows that higher downwash is obtained near the blade tip of the main rotor and slightly off the rotor disk plane due to the interaction with the tail rotor, which subsequently reduces the effective angle of attack for the main rotor blade in this region, compared to the case without the tail rotor.

In Fig. 9, spanwise sectional thrust distributions of the main rotor blade at four azimuth angles are presented, and the results are compared with those of an isolated rotor and the rotor-fuselage configuration. It is shown that all three calculated results are similar to each other, and compare well with the experiment obtained for rotor-alone configuration. However, at Ψ = 0 °, the thrust loading for the configuration with the tail rotor is substantially lower than the other two cases near the blade tip region. This confirms that higher induced downwash exists in the region near the tail rotor, which reduces the effective angle of attack and thus the blade loading.

In Fig. 10, the sectional thrust contours are presented for one revolution of the main rotor. It is shown that a significant distortion of blade loading exists for the rotor azimuth angle between 320° and 15°, due to the interference with the tail rotor as described earlier, which could be a potential source of blade vibration.

3.3 Air-launched Rockets From Complete UH-60 Configuration

Finally, the present overset mesh flow solver was coupled with six degree-of-freedom equations of motion, and numerical simulation of the effect of downwash on air-launched rockets and their plume development was conducted for rockets with and without fin and canard. In Fig. 11, the computational mesh of an UH-60 helicopter with external launcher is presented. The overset mesh was composed of four mesh blocks, which consisted of 837,729, 616,941, and 82,328 vertices for fuselage and launcher, main rotor, and tail rotor, respectively. The last sub-block was used for modeling the rockets, and contained 285,904 and 327,310 vertices for the folded (without canard and fin) and unfolded canard and fin cases, respectively. In Fig. 12, detailed modeling of the rockets and the launcher with seven tubes are presented. In the present calculation, the rocket was launched from the center tube, and other rockets were assumed to reside inside the remaining six tubes.

In Fig. 13, the predicted rotor downwash contours on the horizontal plane where the rocket launcher is located are presented. Also, the downwash distribution along the rocket trajectory, A-A', is presented. It is shown that fairly large variation of downwash exists along the rocket flight trajectory, not only underneath the rotor disk plane but also just off from the rotor, which affects the trajectory and the attitude of the flying rocket, particularly at the initial stage of the launch. The magnitude of the largest downwash was 27.2 m/sec, whereas the downwash by the simple momentum theory was 13.1 m/sec.

In Fig. 14, the behavior of the free-flight rockets is presented. The rockets were fired when the azimuth angle of the main rotor was at zero degree. For the simulation, it was assumed that the plume exhausted from the rocket nozzle produces constant thrust during the flight after initial fire. While moving inside the launcher tube, the rocket was assumed to perform one degree-of-freedom motion. After 0.2 sec from fire, the rocket traveled approximately 9 meters along its longitudinal axis and went out of the main rotor disk plane. The results show that the rocket with fin and canard (unfolded) is in a slight nose-up pitching motion, whereas the rocket without fin and canard (folded) is in a nose-down pitching motion. For both rocket cases, the pitch rate increases most rapidly near and slightly off from the tip of the rotor disk plane, showing the largest influence of rotor downwash. For the rocket with fin and canard, slight yaw angle and side slip velocity were observed due to the asymmetry of the downwash on both sides of the rocket, even though the magnitude is relatively small compared to the pitching motion. In the case of the rocket without canard and fin, the effect of downwash to yaw and side slip is relatively small. As the rockets left the launcher, slight vertical downward displacement was observed for both rocket cases. The displacement is less for the unfolded rocket, because the canard and fin produce some lift at positive pitch attitude. The rockets accelerated along their trajectory after launched from the tube. No significant difference was observed between the two rockets for this axial acceleration.

In Fig. 15, a detailed view of the launch sequence of the rocket after fire is presented in terms of temperature contours. It is shown that right after the rocket nozzle leaves the launcher tube exit, the plume impinges to the launcher front end surface, momentarily forming a high pressure and temperature region. As the rocket moves further away from the launcher, the plume bends down slightly due to rotor downwash, forming a high pressure and temperature region on the bottom part of the launcher front end surface.

In Fig 16, the pressure and temperature variations are presented at the center of the war heads of unfired rockets which remain inside the launcher tubes. It is shown that after the rocket is fired from the center tube, the pressure and temperature significantly increase, particularly at the nose of the rocket inside the bottom tube, due to the downward deflection of the plume. This hot plume gas might cause potential damages to the remaining rockets, disabling the rocket seeker and endangering the safety of the war head.

In Fig. 17, instantaneous surface pressure and temperature contours are presented slightly after the rocket is launched from the launcher pad. It is shown that the launcher pad and the advancing side of the fuselage are significantly affected by the rocket plume flow, experiencing pressure and temperature rise.

4. CONCLUSION

Numerical simulation of unsteady flow fields around rotorcraft configurations was conducted to investigate the aerodynamic interference effect between main rotor, fuselage, tail rotor, and also air-launched rockets. For this purpose, a vertex-centered finite-volume flow solver based on unstructured meshes has been developed. The flow solver has been coupled with six degree-of-freedom equations of motion to describe the trajectory of free-flight rockets. For the validation of the present flow solver, rotor-fuselage aerodynamic interaction of the ROBIN configuration and the mutual interaction of a complete helicopter configuration, UH-60, were calculated. Based on the results of the UH-60 helicopter calculation, free-flight rockets launched from a complete UH-60 helicopter were simulated, and the effect of rotor downwash on the trajectory and the initial behavior of the launched rockets

were investigated. The effect of downwash on the plume development and its impact on other components were also studied. It was found that rotor downwash has non-negligible influence on the rocket trajectory, and the hot gas from the rocket nozzle exit should be seriously considered for the design and development of a safer and more reliable air-launched weapon system in the future.

ACKNOWLEDGMENT

The work was supported by the Agency for Defense Development and the Defense Acquisition Program Administration. The contract number was UD070041AD.

REFERENCES

[1] S. Shanks and J. U. Ahmad, “Aerodynamics of Powered Missile Separation from a Wing,” AIAA Paper 1991-1663, Honolulu, Hawaii, June 1991.

[2] P. A. Cavallo, N. Shinha, and G.M. Feldman, “Parallel Unstructured Mesh Adaptation For Transient Moving Body and Aeropropulsive Applications,” AIAA Paper 2004-1057, Reno, Jan., 2004.

[3] R. B. Taylor and A.J. Landgrebe, “Investigation of the Airflow at Rocket Trajectory and Wind Sensor Locations of a Model Helicopter Simulating Low Speed Flight,” UTRC Report No. R79-912985-5., 1979.

[4] F. S. Wei and J. Gjestvang, “Store Separation Analysis of Penguin Missile from the SH-2G Helicopter,” AIAA Paper 2001-0992, Reno, Jan., 2001.

[5] P. L. Roe, “Approximate Riemann Solvers, Parameter Vectors and Difference,” *Journal of Computational Physics*, Vol.43, (2), 1981, pp. 357-372.

[6] M. S. Jung and O. J. Kwon, “A Parallel Unstructured Hybrid Overset Mesh Technique for Unsteady Viscous Flow Simulations,” Presented at the International conference on Parallel Computational Fluid Dynamics, ParCFD 2007-024, 2007.

[7] M. S. Jung and O. J. Kwon, “A Conservative Overset Mesh Scheme via Intergrid Boundary Reconnection on Unstructured Meshes,” AIAA Paper 2009-3536, San Antonio, TX, June 2009.

[8] K. Nakahashi, F. Togashi, and D. Sharov, “Intergrid-Boundary Definition Method for Overset Unstructured Grid Approach,” AIAA Journal, Vol.38, (11), 2000, pp. 2077-2084.

[9] E. M. Raymond and S. A. Gorton, "Steady and Periodic Pressure Measurements on a Generic Helicopter Fuselage Model in the Presence of a Rotor," NASA TM 2000-210286, 2000.

[10] A. R. Kenyon and R. E. Brown., “Wake Dynamics and Rotor–Fuselage Aerodynamic Interactions,” Presented at the AHS 63rd Annual Forum, Virginia Beach, May 1-3, 2007.

[11] W. G. Bousman, “Aerodynamic Characteristics of SC1095 and SC 1094 R8 Airfoils,” NASA/TP-2003-212265, 2003.

[12] K. B. Hilbert, “A Mathematical Model of the UH-60 Helicopter,” NASA TM 85890, 1984.

[13] B. E. Wake and J. D. Beader, “Evaluation of a Navier-Stokes Analysis Method for Hover Performance Prediction,” *Journal of the American Helicopter Society*, Vol. 41, (1), 1996, pp. 7-17.

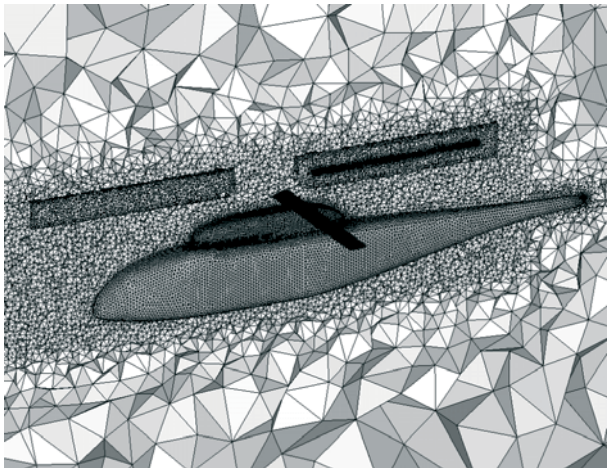

Fig. 1 Mesh distribution on fuselage and blade surface and at fuselage symmetric plane.

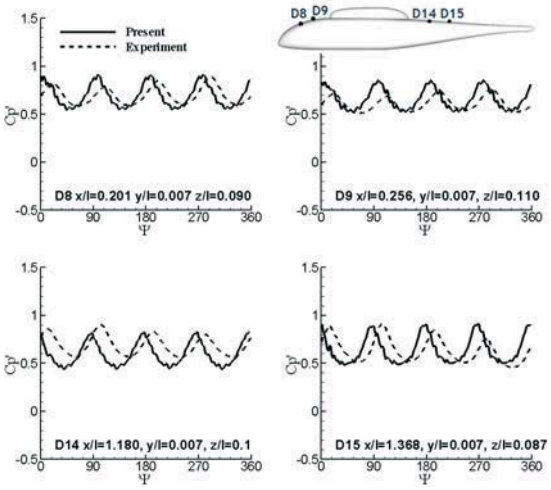

Fig. 2 Unsteady pressure variation along fuselage top center line.

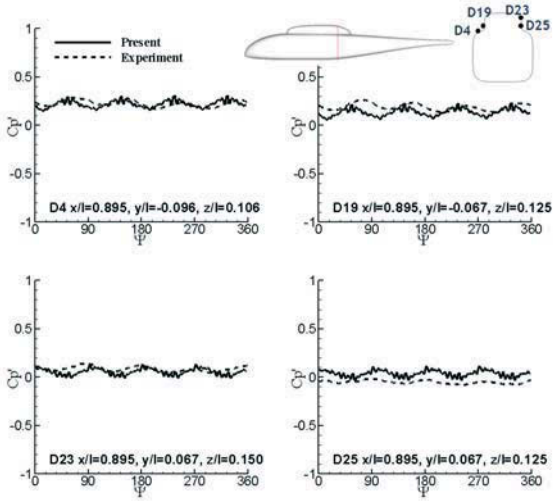

Fig. 3 Unsteady pressure variation around fuselage at x/l=0.9.

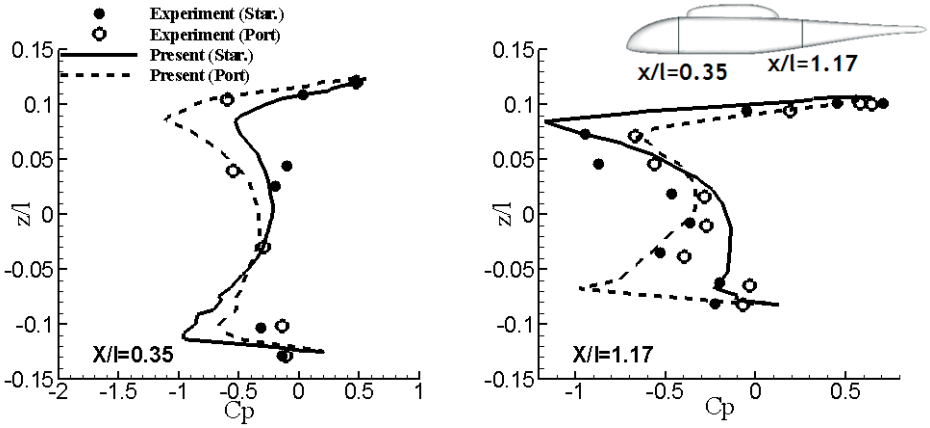

Fig. 4 Time-averaged pressure distribution around fuselage at two selected streamwise stations.

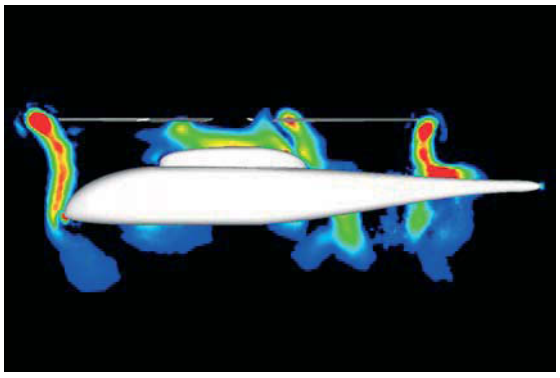

Fig. 5 Instantaneous vorticity contours for blades aligned along $\Psi = 45$ °.

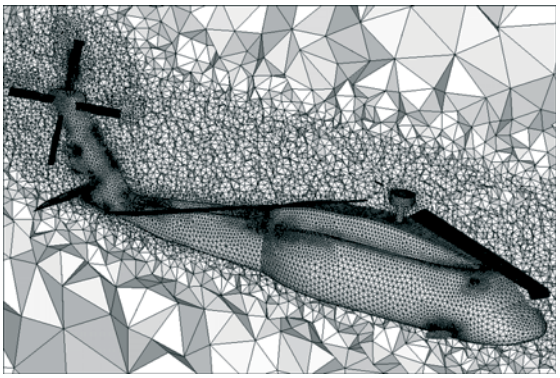

Fig. 6 Computational mesh for complete UH–60 helicopter configuration.

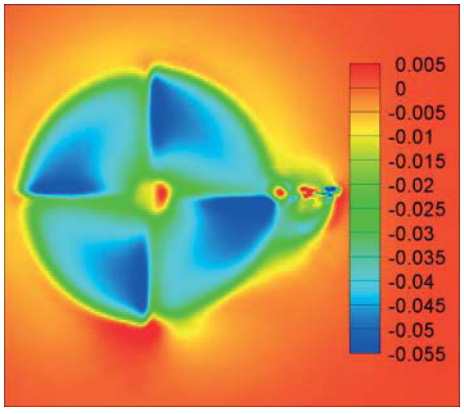

Fig. 7 Inflow contours at one chord length above rotor disk plane.

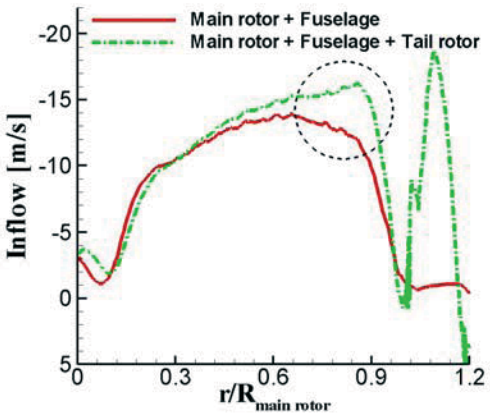

Fig. 8 Inflow distribution along $\Psi = 0$ ° at one chord length above rotor disk plane.

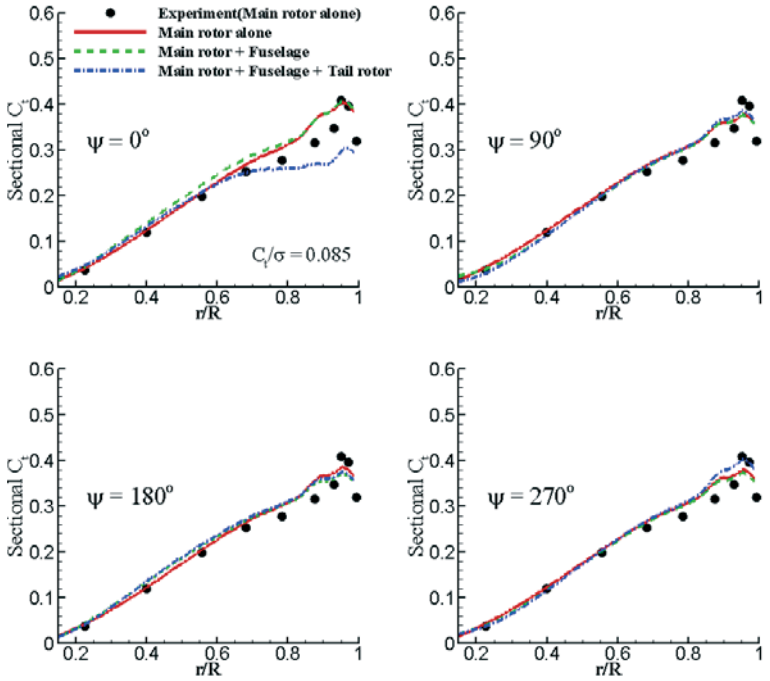

Fig. 9 Spanwise sectional thrust loading distribution on main rotor blade.

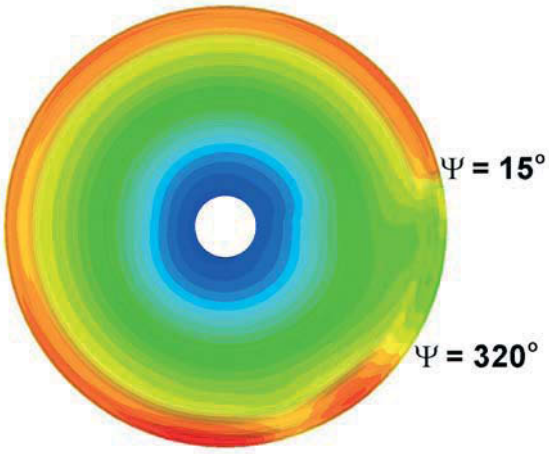

Fig. 10 Sectional thrust contours for one revolution of main rotor.

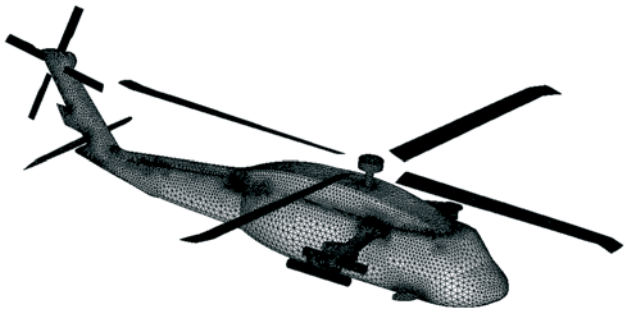

Fig. 11 Surface mesh for complete UH-60 helicopter configuration with rocket launcher installation.

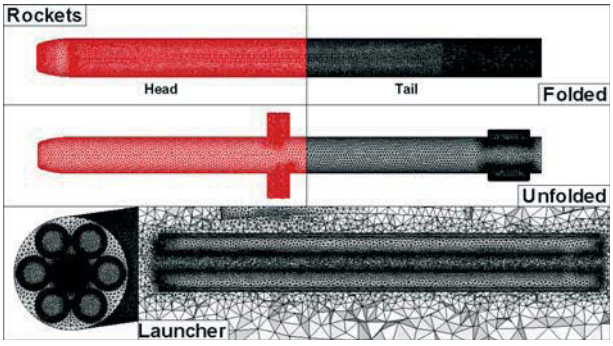

Fig. 12 Detailed modeling of launcher and rockets with and without canard and fin.

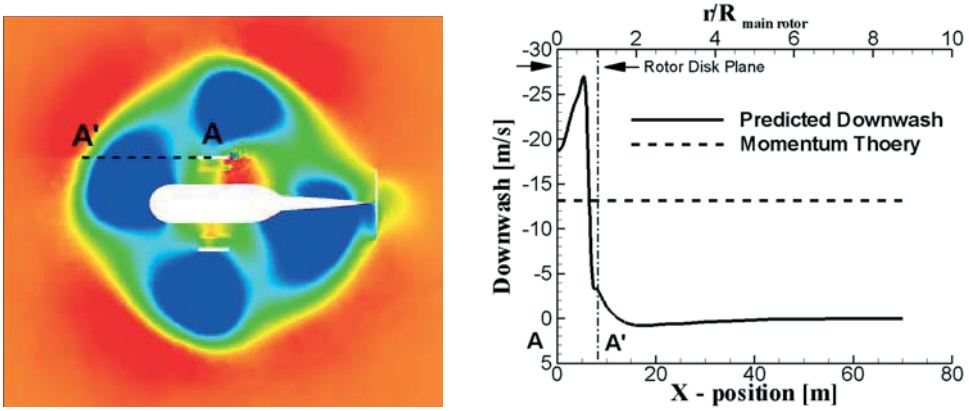

Fig. 13 Predicted rotor downwash distribution at the plane of launcher and along rocket trajectory.

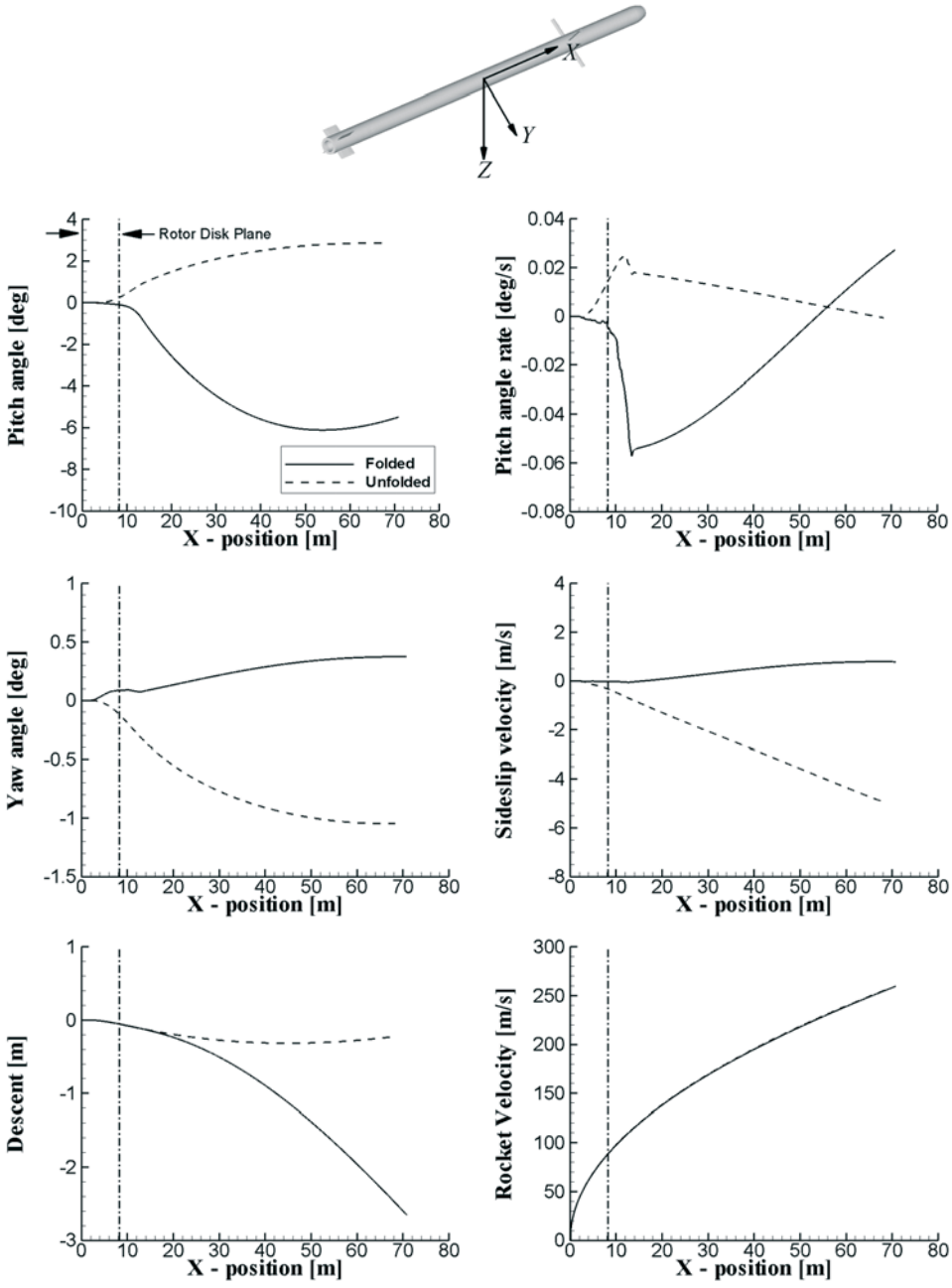

Fig. 14 Trajectory and behavior of air-launched rockets.

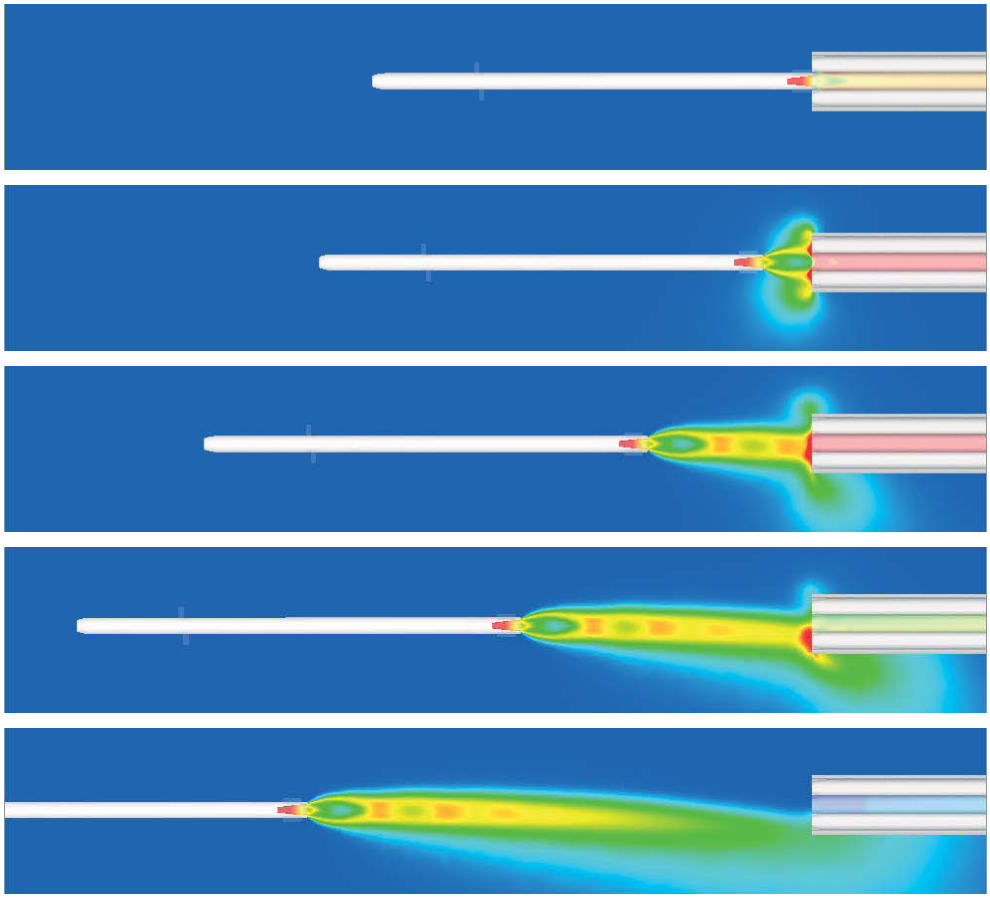

Fig. 15 Temperature contours as launch sequence of fired rocket and plume development.

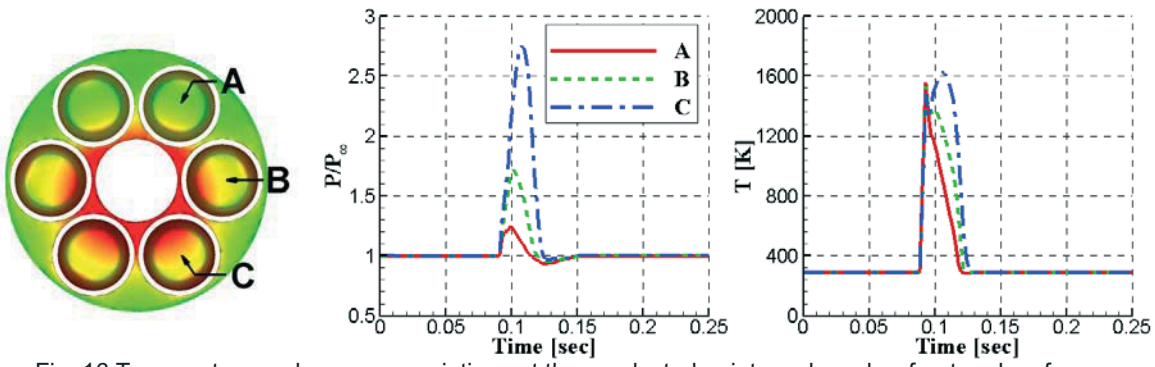

Fig. 16 Temperature and pressure variations at three selected points on launcher front end surface.

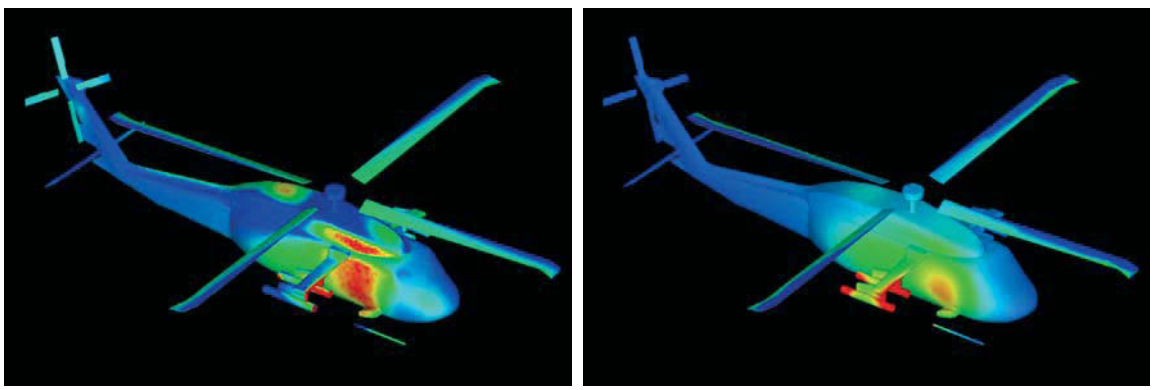

Fig. 17 Instantaneous surface pressure(left) and temperature(right) contours after rocket fire.